

Tailing the Magnetoelectric Properties of Cr<sub>2</sub>Ge<sub>2</sub>Te<sub>6</sub> by Engineering Covalently Bonded Cr Self-Intercalation: Ferromagnetic Half-Metal

Zhaoyong Guan,\* Linhui Lv, Ziyuan An, Yanyan Jiang, and Ya Su

Cite This: *ACS Appl. Electron. Mater.* 2023, 5, 2999–3009

Read Online

ACCESS |



Metrics &amp; More



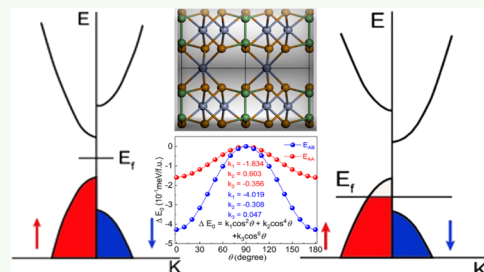
Article Recommendations



Supporting Information

**ABSTRACT:** Two-dimensional intrinsic ferromagnetic half-metals (HMs) are important for spintronics. Based on a systematic research of CrGeTe<sub>3</sub> (CGT) bilayers and multilayers with the self-intercalated (SI) Cr (Cr<sub>SI</sub>) atom, we find that self-intercalation can enhance interlayer magnetic coupling, which results in a super-exchange interaction between interlayers. The CGT bilayer keeps half-metallicity with the interlayer ferromagnetic (FM) order after Cr's self-intercalation, independent of Cr<sub>SI</sub> atoms' concentration and stacking orders. Moreover, SI-CGT multilayers with interlayer FM order transform from HMs into normal spin-polarized metals, as the states at the Fermi level increase. Moreover, the magnetic anisotropy energies (MAEs) of SI-CGT-AA and SI-CGT-AB are  $-0.160$  and  $-0.42$  meV/f.u., respectively, which are modulated by the Cr<sub>SI</sub> atoms. The MAEs of SI-CGT-AA and SI-CGT-AB are different, as the hybridization interactions between Cr's d orbitals are different from each other. SI-CGT bilayers' magnetic easy axis (EA) switches from the original [001] of CGT to the [100] direction, independent of the stacking orders. It is inferred that the MAE is mainly contributed by the hybridization between Te's p<sub>x</sub> and p<sub>y</sub>, p<sub>y</sub> and p<sub>z</sub> orbitals, and that this hybridization interaction is obviously weakened as Cr<sub>SI</sub> atom is inserted. The SI-CGT bilayers and multilayers show good dynamic and thermal stability at 300 and 500 K. These findings offer a promising way to manipulate the interlayer exchange interaction and magnetoelectric properties of CGT multilayers and other vdW magnets.

**KEYWORDS:** self-intercalation, 2D ferromagnetism, half-metal, magnetic crystal anisotropy, magnetic vdW material, EA switch



## INTRODUCTION

Since the discovery of graphene, all kinds of two-dimensional (2D) materials, such as hexagonal boron nitride,<sup>1,2</sup> transition metal dichalcogenides,<sup>3,4</sup> and stanene,<sup>5</sup> have been found. Most 2D materials are nonmagnetic materials,<sup>6,7</sup> as long-range magnetic order is prohibited by the strong fluctuations at finite temperature in 2D materials.<sup>8</sup> Recently, 2D van der Waals (vdW) magnetic materials,<sup>9,10</sup> such as CrI<sub>3</sub> (MI<sub>3</sub>),<sup>11–17</sup> Fe<sub>3</sub>GeTe<sub>2</sub>,<sup>18,19</sup> VS(Se)<sub>2</sub>,<sup>20–22</sup> VSeTe,<sup>23,24</sup> and CGT,<sup>25–30</sup> have attracted much attention. Interlayer magnetic coupling has been confirmed to play an important role in modulating the magnetoelectric properties of magnetic vdW materials. Taking CrI<sub>3</sub> as an example, there are two magnetic orders, which show interlayer ferromagnetic (FM) and antiferromagnetic (AFM) couplings, respectively.<sup>31</sup>

In all kinds of modified methods, intercalation is a useful approach to controlling vdW materials' properties,<sup>32</sup> such as topological properties,<sup>33</sup> photonics,<sup>34</sup> optoelectronic properties,<sup>35,36</sup> thermoelectric properties,<sup>37,38</sup> energy storage,<sup>39,40</sup> catalytic properties,<sup>41</sup> and magnetoelectric properties.<sup>16,17,27,42–50</sup> Apart from foreign atoms, the native atoms could also work as intercalants.<sup>47</sup> This phenomenon is called self-intercalation, which has attracted much attention. The self-intercalated (SI) structures show more stable structures compared with other vdW structures.<sup>32</sup> In addition, the native

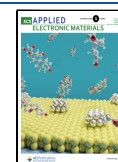
magnetic SI atoms could affect interlayer magnetic coupling.<sup>42,44,51,52</sup> In 2020, researchers successfully synthesized SI structures in TaS(Se)<sub>x</sub> by performing growth under a high metal chemical potential.<sup>50,51</sup> Besides these, V<sub>11</sub>S<sub>16</sub>, In<sub>11</sub>Se<sub>16</sub>, and Fe<sub>x</sub>Te<sub>y</sub> could be synthesized under metal-rich conditions.<sup>50</sup> In 2022, the phase-selective synthesis of trigonal and monoclinic Cr<sub>5</sub>Te<sub>8</sub> crystals was achieved, using chemical vapor deposition.<sup>53</sup> The successful experimental realization in 2D materials<sup>54</sup> paves a new way to modulate the magnetoelectric properties of 2D materials.<sup>50,51,53,55,56</sup>

In this article, by using the first-principles method, we perform a systematic research on the magnetic and electronic properties of SI-CGT bilayers and multilayers. The SI-CGT bilayers are HMs with interlayer FM order, independent of stacking patterns and Cr<sub>SI</sub> atoms' concentration. SI-CGT multilayers are spin-polarized metals with interlayer FM order, irrespective of the stacking patterns and films' thickness. The AB stacking orders have a lower energy when the number of

**Received:** December 21, 2022

**Accepted:** April 21, 2023

**Published:** May 22, 2023



layers is less than five. Moreover,  $\text{Cr}_{\text{SI}}$  atoms could effectively modulate the MAE and even switch EA from [001] to [100] directions, as the hybridization interaction between Te's  $p_x$  and  $p_y$ ,  $p_y$  and  $p_z$  orbitals is obviously weakened. Moreover, the different stacking orders affect the hybridization interaction between Cr atoms'  $d_{xz}$  and  $d_{xy}$ , and  $d_{xy}$  and  $d_{x^2-y^2}$  orbitals, resulting in different MAEs of CGT with SI-AA and SI-AB stackings. SI-CGT multilayers also show good dynamical and thermal stability. These findings offer a promising way to manipulate the interlayer exchange interaction and magneto-electric properties of CGT multilayers and other vdW magnets.

## COMPUTATIONAL DETAILS

The calculation of SI-CGT is done using the plane-wave basis Vienna Ab initio Simulation Package (VASP) code,<sup>57</sup> based on the density functional theory. The generalized gradient approximation (GGA) with Perdew–Burke–Ernzerhof (PBE)<sup>58</sup> is adopted. The GGA +  $U$  method<sup>59</sup> and hybrid-functional HSE06<sup>60,61</sup> are used to deal with the strong-correlated correction to Cr's 3d electrons. The effective onsite Coulomb interaction parameter ( $U$ ) and exchange interaction parameter ( $J$ ) are set to be 3.60 and 0.60 eV, respectively. Therefore, the effective  $U_{\text{eff}}$  ( $U_{\text{eff}} = U - J$ ) is set to be 3.0 eV.<sup>62,63</sup> The change of MAEs with  $U_{\text{eff}}$  is also tested, as shown in Figure S1 in the Supporting Information. The geometry optimization, energies with all kinds of magnetic orders, band structure, density of the states (DOS), phonon spectrum, ab initio molecular dynamics (AIMD), and MAEs are calculated with the LDA +  $U$  method. Energies with all kinds of magnetic orders, spin charge densities difference, and DOS are confirmed using the HSE06 functional. The vacuum space in the  $z$ -direction is set to be 16 Å to avoid virtual interaction. The kinetic energy cutoff is set as 360 eV. The geometries are fully relaxed until the energy and force are converged to  $10^{-5}$  eV and 1 meV/Å, respectively.  $9 \times 9 \times 1$  and  $12 \times 12 \times 1$  Monkhorst–Pack grids<sup>64</sup> are used for the geometry optimization and energy calculation, respectively. Spin–orbital coupling (SOC) is also considered in the calculation of MAE and band structures.

MAE was calculated to have an energy cutoff of 400 eV. The convergence of total energy and force is  $1 \times 10^{-8}$  eV and  $1 \times 10^{-3}$  eV/Å, respectively. Based on the systematic test, the corresponding  $k$ -grid adopted is  $21 \times 21 \times 1$ , without any symmetry constriction, as shown in Figure S2. The phonon spectra and DOS are calculated using the finite displacement method as implemented in Phonopy software Package.<sup>65</sup> A  $2 \times 2 \times 1$  cell is adopted in the simulation, and the total energy and Hellmann–Feynman force are converged to  $10^{-8}$  eV and 1 meV/Å, respectively. In total, 6000 uniform  $k$ -points along high-symmetry lines are used to obtain the phonon spectra. Moreover, AIMD simulation is also performed to confirm the structural stability. The constant moles–volume–temperature (NVT) ensemble with Nosé–Hoover thermostat<sup>66</sup> is adopted at temperatures of 300 and 500 K, respectively. The time step and total time are 1 fs and 10 ps, respectively. In order to eliminate the effect of periodic boundary condition with a relatively smaller system size, a larger supercell ( $2 \times 2 \times 1$  cell) is used in the AIMD simulation. The DFT-D2 Grimme method<sup>67</sup> is adopted to describe the weak vdW interaction between layers, and DFT-D3 Grimme<sup>68</sup> is also used to confirm the key results.

The climbing image-nudged elastic band (CI-NEB) method<sup>69</sup> is used to calculate the migration barrier of the

$\text{Cr}_{\text{SI}}$  atom. The atomic positions are fully relaxed with a force criterion of 0.03 eV/Å<sup>-1</sup> for all intermediates and transition states. Six images are inserted between the reactant and the product.

## RESULTS AND DISCUSSION

**Geometry of the SI-CGT Monolayer (ML).** There are two different stacking orders, AA and AB, for the CGT bilayer. Therefore, when  $\text{Cr}_{\text{SI}}$  atoms are embedded, there are two kinds of structures, named AA-SI and AB-SI, as shown in Figure 1a–

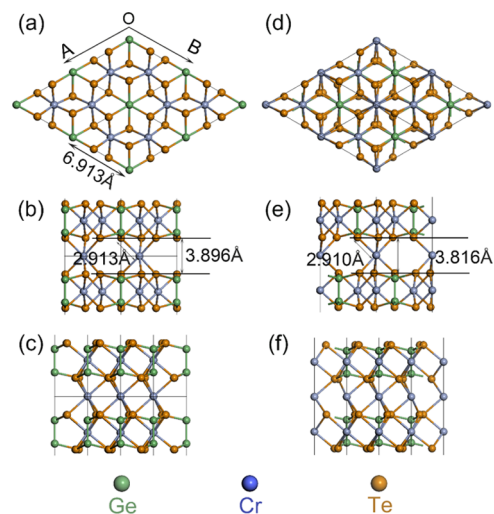


**Figure 1.** (a, d) Top, (b, e) side-1, and (c, f) side-2 views of the optimized geometry of 111-AA-SI-2 and 111-AB-SI-2. The green, blue, and yellow balls represent Ge, Cr, and Te atoms, respectively.

f. The geometries of AA-SI and AB-SI are fully optimized by the LDA +  $U$  method. The 111-AA(AB)-SI-2 layer are defined as follows: CGT comprising a  $1 \times 1 \times 2$  cell (bilayer) with  $\text{Cr}_{\text{SI}}$  atoms stacked with AA (111-AA-SI-2) and AB (111-AB-SI-2). The 111-AA-SI bilayer (111-AA-SI-2) shows a  $D_{3D}$  point group, while the 111-AB-SI bilayer (111-AB-SI-2) shows a  $C_3$  point group, as shown in Figure 1a–f, respectively. Both 111-AA-SI-2 and 111-AB-SI-2 have the same lattice parameter ( $a = b$ ) of 6.913 Å, as shown in Figure 1a,d. The lattice parameters of AA-SI and AB-SI are similar to those of CGT of 6.910 Å.<sup>10</sup> The vertical distance between the Te atoms of different layers is 3.896 Å (111-AA-SI-2) and 3.816 Å (111-AB-SI-2), respectively. The vertical distance between the Te atoms of 111-AA-SI-2 is smaller than the bilayers with an AA stacking of 4.220 Å, while the distance between the atoms of 111-AB-SI-2 is bigger than the bilayer with AB stacking of 3.698 Å. The distance between  $\text{Cr}_{\text{SI}}$  and the nearby Te atoms is 2.910 Å, respectively. The  $\text{Cr}_{\text{SI}}$  atom tends to locate at hollow site of the top and bottom layers, as shown in Figure 1. The corresponding angles between  $\text{Cr}_{\text{SI}}$  and Te atoms of 111-AA-SI-2 are 105.59, 94.79, and 80.16°, while the angles are 81.41, 98.59, and 98.59° for 111-AB-SI-2, respectively. The intralayer of AA-SI-2 and AB-SI-2 keeps the original structure, without obvious distortion, as shown in Figure 1a–f. The geometries of 111-AA-SI-2 and 111-AB-SI-2 are also optimized by the DFT-D3 method, as shown in Figure S3a,b, respectively, and the distance between  $\text{Cr}_{\text{SI}}$  and the nearby Te atoms is a little smaller than found by the DFT-D2 method. More details could be found in the Supporting Information.

**Magnetic and Electronic Properties.** The geometries of SI-CGT were investigated, and magnetic properties were found to be usually related with the geometries. In this section, the magnetic properties are studied. The magnetic moment (MM) mainly localizes at the Cr atoms, as shown in Figure 2a–f. In

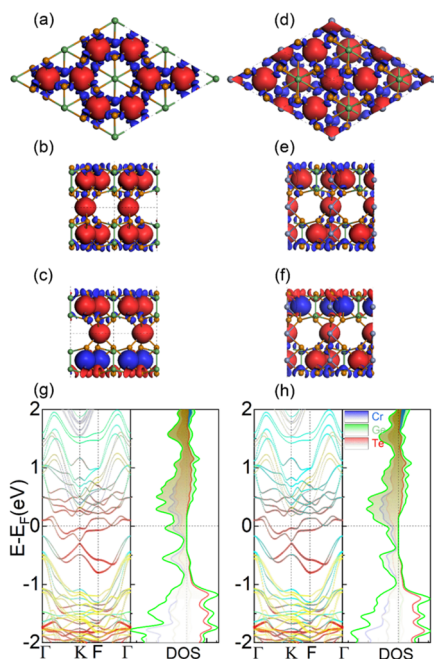


**Figure 2.** Spin charge density difference of 111-AA-SI-2 with interlayer (a, b) FM and (c) AFM orders. The spin charge difference density of 111-AB-SI-2 with interlayer (d, e) FM and (f) AFM orders. Spin-polarized band structure and PDOS of (g) 111-AA-SI-2 and (h) 111-AB-SI-2 with FM order. The red, gray, green, blue, cyan, and yellow colors represent Cr- $\alpha$ , Cr- $\beta$ , Ge- $\alpha$ , Ge- $\beta$ , Te- $\alpha$ , and Te- $\beta$  atoms' projected band structures, respectively. The blue, green, and red colors present Cr, Ge, and Te atoms' PDOS of SI-CGT.

order to confirm the magnetic ground state, eleven magnetic orders are considered, as shown in Figure S4a,b. It can be concluded that 111-AA-SI-2 and 111-AB-SI-2 show an interlayer FM ( $\text{FM}_{\text{FM-FM}}$ ) order. The interlayer  $\text{FM}_{\text{FM-FM}}$  order is defined as follows: the Cr atoms of the intralayer (1st L) ferromagnetically couple with other Cr atoms (1st L), and the Cr atoms of the interlayer (2nd L) ferromagnetically couple with other Cr atoms (1st L), as shown in Figure 2a,b,d,e. The interlayer AFM ( $\text{AFM}_{\text{FM-FM}}$ ) order is defined as follows: the Cr atoms of the intralayer (1st L) ferromagnetically couple with other Cr atoms, while the Cr atoms of the interlayer antiferromagnetically couple with other Cr atoms (2nd L), as shown in Figure 2c,f. The corresponding energy difference ( $\Delta E$ ) between interlayer FM and AFM orders is defined to describe the magnetic stability of materials:  $\Delta E = E_{\text{FM}} - E_{\text{AFM}}$ . The energies of 111-AA-SI-2 and 111-AB-SI-2 with interlayer FM order are 0.266 and 0.278 eV lower than the interlayer  $\text{AFM}_{\text{FM-FM}}$  order, which indicates that they show interlayer FM order. The corresponding  $\Delta E$  is  $-0.266$  and  $-0.278$  eV, respectively. However, the  $\Delta E$  of the CGT bilayer without  $\text{Cr}_{\text{SI}}$  atoms is  $-2.680$  (111-AA-2) and  $-4.371$  meV (111-AB-2), respectively.<sup>10</sup> It can be concluded that the  $\text{Cr}_{\text{SI}}$  atoms could obviously enhance the ferromagnetism of CGT, as the super-exchange interaction between Cr atoms is strengthened. The differential charge density is defined as

follows:  $\text{CGT-SICGT-1}^{\text{st}}\text{LCGT-2}^{\text{nd}}\text{LCr-SI}$ . Charges accumulate and deplete at  $\text{Cr}_{\text{SI}}$  atoms, as found by analyzing the differential charge density and shown in Figure S3a–d in the Supporting Information. It can be found that the  $\text{Cr}_{\text{SI}}$  atom loses 0.78 (0.73)  $e$  electron to the nearby Te atoms as found by the Bader analysis.<sup>70</sup> Te atoms (1st L) of 111-AA-SI-2 bonded to the  $\text{Cr}_{\text{SI}}$  atom lose 1.075, 1.253, and 1.233  $e$  electrons, and Te atoms (2nd L) lose 1.228, 1.277, and 1.280  $e$  electrons, respectively. Moreover, Te atoms (1st L) of 111-AB-SI-2 lose 1.626, 1.352, and 1.267  $e$  electrons, and Te atoms (2nd L) lose 1.503, 1.206, and 1.274  $e$  electrons, respectively. More details could be found in the Supporting Information. The Cr atom has a  $d^5s^1$  configuration, and one d electron and s electron are lost. As a result, the Cr atoms of 111-AA-SI-2 with interlayer FM order have 3.911 (1st L), 3.683 (1st L), 4.180 ( $\text{Cr}_{\text{SI}}$ ), 3.911 (2rd L), and 3.683 (2rd L)  $\mu_{\text{B}}$  MM, respectively. For 111-AB-SI-2, the Cr atoms have 3.915 (1st L), 3.683 (1st L), 4.160 ( $\text{Cr}_{\text{SI}}$ ), 3.915 (2rd L), and 3.683 (2rd L)  $\mu_{\text{B}}$  MM. Further, more magnetic orders and corresponding energies were calculated, as shown in Figure S4a,b, respectively. Both 111-AA-SI-2 and 111-AB-SI-2 show the interlayer FM ground state by considering the magnetic orders. In a word, the super-exchange interaction plays an important role in interlayer magnetic exchange interaction.

The electronic properties are usually related to magnetic orders. The band structures of 111-AA-SI-2 and 111-AB-SI-2 with interlayer FM order are calculated, as shown in Figure 2g,h, respectively. There are two sub-bands of 111-AA-SI-2 crossing the Fermi level for spin- $\alpha$  electrons. Also, these states at Fermi level are mainly contributed by the Cr and Te atoms, as shown in Figure 2g,h. Therefore, the spin- $\alpha$  electrons are conducting. However, 111-AA-SI-2 is a semiconductor with an indirect band gap of 0.682 eV for spin- $\beta$  electrons. In a word, 111-AA-SI-2 is an HM. A similar phenomenon also appears in 111-AB-SI-2. The spin- $\alpha$  electrons of 111-AB-SI-2 are conducting, while spin- $\beta$  electrons are semiconducting. Therefore, 111-AB-SI-2 is also an HM. Other stacking orders are tested, and they are all HMs with interlayer FM order, independent of stacking orders. In sum, both 111-AA-SI-2 and 111-AB-SI-2 are HMs with interlayer FM order, and the states near the Fermi level are mainly contributed by Cr atoms, as shown in Figure 2g,h, respectively.

In order to clarify Cr's magnetic moment, d electrons' PDOS and integrated density of the states (IDOS) were calculated, shown in Figure 3. The corresponding Cr-projected PDOS are shown in Figure 3a,b. The  $d_{x^2-y^2}$ ,  $d_z^2$ ,  $d_{yz}$ ,  $d_{xz}$ , and  $d_{xy}$  orbitals of 111-AA-SI-2 are partially occupied by the spin- $\alpha$  electrons, as shown in Figure 3a,c. Moreover, the  $d_{yz}$  and  $d_{xz}$  orbitals of 111-AA-SI-2 are degenerate, as shown in Figure 3a,c. The  $d_{x^2-y^2}$  and  $d_{xy}$  orbitals of 111-AA-SI-2 are also degenerate, as shown in Figure 3a,c. A similar trend also appears in 111-AB-SI-2, as shown in Figure 3b,d. For 111-AB-SI-2, the  $d_{yz}$  and  $d_{xz}$  orbitals are degenerate, which make a main contribution to the d-orbital. In addition,  $d_{x^2-y^2}$  and  $d_{xy}$  orbitals are also degenerate, as shown in Figure 3b,d, respectively. In fact, other stacking orders are also tested, which show a similar trend. In a word, all  $d_{x^2-y^2}$ ,  $d_{xy}$ ,  $d_{yz}$ , and  $d_{xz}$  orbitals are degenerate.

Moreover, the electronic properties are usually related to the magnetic orders. Both 111-AA-SI-2 and 111-AB-SI-2 show interlayer FM order. The band structures with other magnetic orders were also calculated, as shown in Figures S5, S6, respectively. 111-AA-SI-2 with interlayer  $\text{FM}_{\text{FM-FM}}$  interlayer

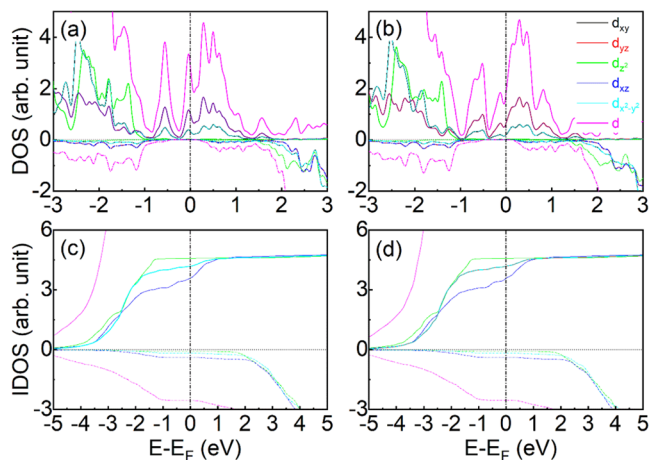


**Figure 3.** Cr's d-orbital projected DOS of (a) 111-AA-SI-2 and (b) 111-AB-SI-2; IDOS of (c) 111-AA-SI-2 and (d) 111-AB-SI-2 with the FM order. The black, red, green, blue, cyan, and pink colors represent  $d_{xy}$ ,  $d_{yz}$ ,  $d_z^2$ ,  $d_{xz}$ ,  $d_{x^2-y^2}$ , and total d orbitals' projected DOS, respectively. The solid and dashed lines represent spin- $\alpha$  and spin- $\beta$  electrons, respectively.

AFM<sub>FM-FM</sub> (Figure S5c), and +---- (1st L-SI-2nd L) (Figure S5g) orders are HMs, while other orders are normal spin-polarized metals, as shown in Figure S5 in the Supporting Information. However, only 111-AB-SI-2 with interlayer FM<sub>FM-FM</sub> order is a HM, while other orders are normal spin-polarized metals, as shown in Figure S6. More details and discussion are shown in Figures S5, S6, respectively.

In order to confirm the validity of vdW-corrected functionals, other vdW-corrected functionals are also adopted. The results of the DFT-D3 method are shown in Figure S7. The spin charge density difference of 111-AA-SI-2 and 111-AB-SI-2 are shown in Figure S7a,b, which is the same as for DFT-D2. Both 111-AA-SI-2 and 111-AB-SI-2 are HMs with interlayer FM order, as shown in Figure S7c,d. More details could be found in Figure S7 in the Supporting Information.

The method of HSE06 functional is also used to calculate the spin charge density difference and PDOS of 111-AA(AB)-SI-2, as shown in Figure S8a–f. Both 111-AA-SI-2 and 111-AB-SI-2 show interlayer FM order, and the corresponding  $\Delta E$  is  $-28.3$  and  $-30.1$  meV, as shown in Figure S8a–d. 111-AB-SI-2 has a lower energy than 111-AA-SI-2, which is consistent with the PBE +  $U$  method. The corresponding PDOS are shown in Figure S8e,f, and they are all HMs, independent of the stacking patterns. However, spin- $\beta$  electrons' gap calculated by HSE06 is 1.238 eV, which is larger than that for PBE +  $U$  (0.682 eV). More details could be found in the Supporting Information.

There is Cr atom in CGT, so the effect of SOC on the electronic properties should be considered. The band structure with SOC is also calculated, as shown in Figure S9 in the Supporting Information. There is a Dirac cone at K point, as the magnetic axis is along the [100] direction. The band structures with SOC show metallicity, independent of SI-CGT bilayers' stacking orders, as presented in Figure S9.

#### Properties of Different Concentrations of Cr<sub>SI</sub> Atoms.

In order to investigate the electronic properties of different Cr<sub>SI</sub> atom concentrations, larger  $N \times N \times 1$  ( $N = \sqrt{3}, 2, \sqrt{7}, 3, 4, 5, 6$ ) supercells are fabricated. The corresponding Cr<sub>SI</sub> atom concentrations ( $x$ ) are 33.33, 25, 14.29, 11.11, 6.25, 4, and 2.78%, whose  $\Delta E$  of NN1-AA-SI-2 is  $-0.285$ ,  $-0.223$ ,

$-0.267$ ,  $-0.275$ ,  $-0.159$ ,  $-0.128$ , and  $-0.176$  eV, respectively, shown in Figures 4a and S10. For NN1-AB-SI-2, the

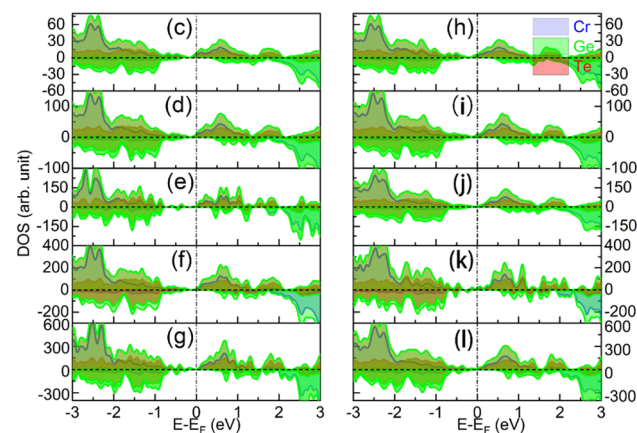
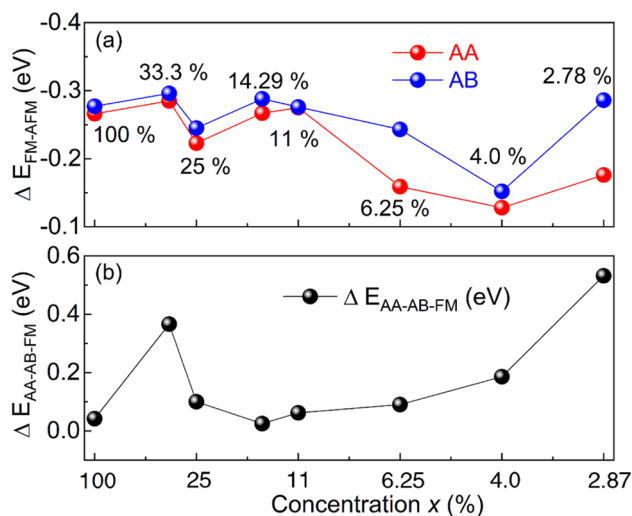


**Figure 4.** Change of (a)  $\Delta E_{FM-AFM}$  and (b)  $\Delta E_{AA-AB-FM}$  with the concentration of Cr<sub>SI</sub> atoms. The PDOS of NN1-AA-SI-2 with  $N$  equals (c) 2, (d) 3, (e) 4, (f) 5, and (g) 6. The PDOS of NN1-AB-SI-2 with  $N$  equals (h) 2, (i) 3, (j) 4, (k) 5, and (l) 6 under the FM order. The Fermi level is set to 0 eV.

corresponding  $\Delta E$  is  $-0.296$ ,  $-0.245$ ,  $-0.288$ ,  $-0.276$ ,  $-0.243$ ,  $-0.152$ , and  $-0.286$  eV, respectively.  $\Delta E$  is always negative, which implies NN1-AA-SI-2 and NN1-AB-SI-2 show interlayer FM order, independent of  $x$ . Moreover, the  $\Delta E$  of NN1-AA-SI-2 is always smaller than NN1-AB-SI-2. The energy difference ( $\Delta E_{AA-AB-FM}$ ) between  $E_{AA-FM}$  and  $E_{AB-FM}$  is defined as follows

$$\Delta E_{AA-AB-FM} = E_{AA-FM} - E_{AB-FM} \quad (1)$$

The  $\Delta E_{AA-AB-FM}$  is 0.042, 0.366, 0.10 and 0.025 eV for  $N = 1, \sqrt{3}, 2, \sqrt{7}$ , respectively. As  $x$  is further decreased, the corresponding  $\Delta E_{AA-AB-FM}$  is 0.062, 0.09, 0.186, and 0.532 eV, respectively, for  $N = 3, 4, 5, 6$ . The  $\Delta E_{AA-AB-FM}$  is always positive, which implies NN1-AB-SI-2 is always more stable than the corresponding NN1-AA-SI-2, shown in Figure 4b. This trend also appears in the bulk of CGT.<sup>10</sup>

As  $x$  is decreased, the corresponding electronic properties also change, as shown in Figure 4c–l, respectively. The PDOS of 221-AA-SI-2 and 221-AB-SI-2 show DOS at Fermi level ( $DOS_F$ ) of 9.272 and 6.950 states/eV, respectively. As  $x$  is

further decreased, the corresponding  $\text{DOS}_F$  are 11.559 (9.974) and 12.256 (13.985) states/eV for  $N = 3, 4$ , as shown in Figure 4d,e,i,j, respectively. As  $x$  is decreased to 4.0 and 2.78%, the corresponding  $\text{DOS}_F$  are 13.635 (16.091) and 12.612 (17.450) states/eV, as shown in Figure 4f,g,k,l, respectively. In a word, all spin- $\alpha$  electrons are conducting, while all spin- $\beta$  electrons are semiconducting. Therefore, all considered geometries show half-metallic with interlayer FM order, independent of  $\text{Cr}_{\text{SI}}$  atom concentration.

**Magnetic Anisotropy Properties.** MAE is often used to describe the magnetic stability of materials, and a larger MAE is highly expected in HMs. A larger MAE means electrons need more energy to overcome a “higher” barrier from EA to the hard axis. In this part, the MAE of CGT and SI-CGT was calculated using the LDA +  $U$  method with SOC. The corresponding energy ( $\Delta E_0$ ) along a certain direction ( $\theta, \phi$ ) follows the below equations

$$\Delta E_0 = K_1 \cos^2 \theta + K_2 \cos^4 \theta + K_3 \cos^6 \theta + K_4 \cos 3\phi \quad (2)$$

$$\Delta E_0 = E - E_{[001]} \quad (3)$$

$E_{[001]}$  represents the energy along the magnetic axis of the [001] direction.  $K_1, K_2,$  and  $K_3$  stand for the quadratic, quartic, and sextic (six degree) contributions to the MAE, respectively.  $\phi$  represents the azimuthal angle, while  $\theta$  represents the polar angle. 111-AA-2 and 111-AA-SI-2 have a  $D_3$  point group, while 111-AB-2 and 111-AB-SI-2 have a  $C_3$  point group. As a result, the energy difference  $\Delta E_0$  is independent of the in-plane azimuthal angle  $\phi$ ,<sup>16,17,27</sup> and the energies with EA along the [100] and [010] directions are the same.<sup>27</sup> In consequence,  $K_4$  equals 0, as shown in Figures S11b,c and 5a,b. Therefore, eq 3 is simplified into the following equation

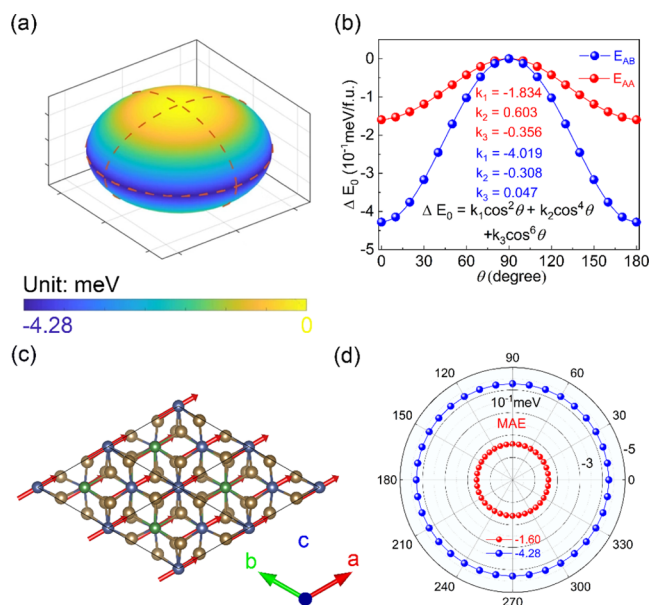


**Figure 5.** MAE map (interlayer FM state as a reference with EA along [100]) of (a) 111-AA-SI-2. The energy indicated by the dashed lines changes with the azimuthal angle  $\phi$ . (b)  $\Delta E_0$  of 111-AA-SI-2 and 111-AB-SI-2 varies from out-of-plane to in-plane direction. (c) Red arrow represents the direction of EA (along the [100] direction) of the 111-AA-SI-2 bilayer. (d)  $\Delta E_0$  changes with polar angle  $\theta$ . Red and blue lines represent 111-AA-SI-2 and 111-AB-SI-2, respectively.

$$\Delta E_0 = K_1 \cos^2 \theta + K_2 \cos^4 \theta + K_3 \cos^6 \theta \quad (4)$$

$\Delta E_0$  changes with functions  $\phi$  and  $\theta$ , as shown in Figure 5a,b and S11b,c, respectively. For 111-AA-2 and 111-AB-2,  $\Delta E_0$  follows the equations  $\Delta E_0(\text{meV}) = 1.79 \cos^2 \theta + 0.010 \cos^4 \theta$  and  $\Delta E_0(\text{meV}) = 1.89 \cos^2 \theta + 0.016 \cos^4 \theta$ , as shown in Figure S11b. Compared with  $k_2, k_1$  is much larger, which means the quadratic part makes the main contribution to the MAE. When  $\text{Cr}_{\text{SI}}$  atoms are embedded into CGT bilayers, the  $\Delta E_0$  of 111-AA-SI-2 follows the equation  $\Delta E_0(10^{-1} \text{ meV}) = -1.834 \cos^2 \theta + 0.603 \cos^4 \theta - 0.356 \cos^6 \theta$ . As for 111-AB-SI-2,  $\Delta E_0$  follows the equation  $\Delta E_0(10^{-1} \text{ meV}) = -0.4019 \cos^2 \theta - 0.308 \cos^4 \theta - 0.047 \cos^6 \theta$ , as shown in Figure 5b.  $k_1$  is  $-0.183$  and  $-0.4019$  meV, while  $k_2$  is  $0.0603$  and  $-0.0308$  meV, respectively. Compared with  $k_2$  and  $k_3, k_1$  is much larger, which is similar to CGT, as shown in Figure S11b. According to Figure 5b, MAE could be calculated by the following equation<sup>27</sup>

$$\text{MAE} = E_{[100]} - E_{[001]} \quad (5)$$

The corresponding MAEs of CGT with 111-AA-2 and 111-AB-2 stackings are 1.80 and 1.91 meV/f.u., as shown in Figure S11c, respectively. The positive MAE implies EA is along the out-of-plane direction, that is, parallel to the  $c$ -axis, which indicates perpendicular magnetic anisotropy (PMA), as shown in Figure S11a.<sup>10</sup> When  $\text{Cr}_{\text{SI}}$  atoms are inserted, the corresponding MAEs of 111-AA-SI-2 and 111-AB-SI-2 are  $-0.160$  and  $-0.428$  meV/f.u., respectively, as shown in Figure 5d. The negative MAE implies EA is along the in-plane direction, which corresponds to in-plane anisotropy (IPA), as shown in Figure 5c. The MAE transforms from positive to negative, which means EA is switched from out-of-plane to in-plane when the  $\text{Cr}_{\text{SI}}$  atoms are introduced.

The MAE of SI-CGT is related to the stacking orders, and the MAE of 111-AB-SI-2 is larger than that of 111-AA-SI-2. This is due to the different hybridization interactions between the Cr orbitals of stacking patterns. Additionally, the EA of 111-AA-SI-2 and 111-AB-SI-2 tends toward IPA, which is different from the PMA of CGT bilayers. This is caused by the  $\text{Cr}_{\text{SI}}$  atom; more discussion could be found in the other part (Magnetocrystalline Anisotropy).

**Multilayers with SI.** When CGT ML was stacked together, it could form multilayers with all kinds of stacking patterns. In this section, the magnetic and electronic properties of stacking multilayers with  $\text{Cr}_{\text{SI}}$  atoms are systematically investigated. As the layer number is increased to three, 111-AA-SI-3 and 111-AB-SI-3 are fabricated, and the corresponding  $\Delta E_0$  is 0.49 and 0.51 eV, respectively. When layer numbers ( $N$ ) are further increased to four, five, and six, the corresponding  $\Delta E$  is 0.792 (AB 0.812), 1.003 (1.026), and 1.272 (1.362) eV, as shown in Figure 6a. When  $N = 7, 8, 9, 10$ , the corresponding  $\Delta E$  is 1.495 (1.570), 1.777 (1.914), 2.004 (2.099), and 2.215 (2.356) eV, respectively. Perhaps more interestingly,  $\Delta E_{\text{AA}}$  and  $\Delta E_{\text{AB}}$  follow the equations  $\Delta E_{\text{AA}} = -0.223 + 0.247N$  and  $\Delta E_{\text{AB}} = -0.258 + 0.264N$ . As the film thickens, both  $\Delta E_{\text{AA}}$  and  $\Delta E_{\text{AB}}$  monotonously increase, as shown in Figure 6a.

$\Delta E_{\text{AA-AB-FM}}$  also changes with the films' thickness, as shown in Figure 6b. When  $N$  equals 2, 3, 4, the corresponding  $\Delta E_{\text{AA-AB-FM}}$  is 0.042, 0.048, and 0.051 eV, respectively. The positive  $\Delta E_{\text{AA-AB-FM}}$  means 111-AA-SI- $N$  is higher than 111-AB-SI- $N$  in energy. More interestingly, as  $N$  is increased to 5,  $\Delta E_{\text{AA-AB-FM}}$  becomes  $-0.084$  eV, which means 111-AA-SI-5 is more stable than 111-AB-SI-5, as shown in Figure 6b. As the

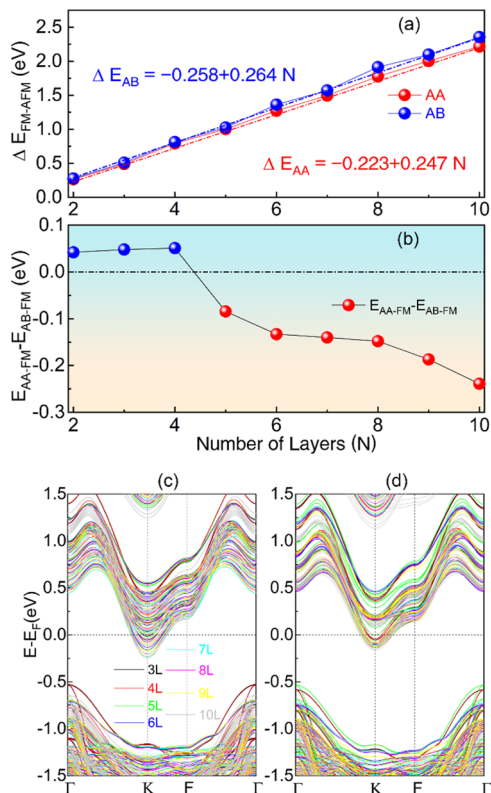


**Figure 6.** (a)  $\Delta E$  and (b)  $\Delta E_{AA-AB-FM}$  change with layers. The spin-polarized band structures of (c) 111-AA-SI- $N$  and (d) 111-AB-SI- $N$  ( $N = 3-10$ ) with the FM order. The black, red, green, blue, cyan, pink, yellow, and gray colors represent  $N$  equal 3, 4, 5, 6, 7, 8, 9, and 10, respectively. The Fermi level is set as 0 eV.

film becomes much thicker, the corresponding  $\Delta E_{AA-AB-FM}$  monotonously increases to  $-0.133$  ( $N = 6$ ),  $-0.14$  ( $N = 7$ ),  $-0.148$  ( $N = 8$ ),  $-0.187$  ( $N = 9$ ), and  $-0.239$  eV ( $N = 10$ ). It can be concluded that 111-AA-SI- $N$  stacking patterns are more stable than 111-AB-SI- $N$  stacking patterns as the film becomes thicker ( $N \geq 5$ ).

The band structures of 111-AA-SI- $N$  and 111-AB-SI- $N$  are also investigated, as shown in Figure 6c,d, respectively. As  $N = 3$ , both spin- $\alpha$  and spin- $\beta$  electrons become conducting, which means 111-AA-SI-3 and 111-AB-SI-3 transform from HM ( $N = 2$ ) into normal spin-polarized metal with interlayer FM order, as shown in Figure 6c. PDOS are also calculated, as shown in Figure S12a,b in the Supporting Information. As the film becomes thicker, the states at Fermi level also increase, as shown in Figure 6c,d. Taking  $N = 4, 6, 8, 10$  as examples, the  $DOS_F$  of spin- $\beta$  electrons are 0.452 (0.985), 0.598 (1.726), 0.965 (2.156), and 1.215 (2.981) states/eV for 111-AA-SI- $N$  and 111-AB-SI- $N$ , respectively. Therefore, 111-AA-SI- $N$  and 111-AB-SI- $N$  ( $N \geq 3$ ) have changed to normal spin-polarized metal with interlayer FM order, as shown in Figure 6c,d, respectively. The PDOS of 111-AA-SI- $N$  and 111-AB-SI- $N$  ( $N = 3,4$ ) are also calculated by HSE06, as shown in Figure S13a-d in the Supporting Information. They are all HMs with interlayer FM order independent of the stacking patterns.

**Dynamic and Thermal Stability.** The dynamic stability of SI-CGT was confirmed via phonon dispersion curves and phonon DOS, which show no obvious imaginary phonon modes. The highest vibration frequency is 8.020 and 8.018 THZ for 111-AA-SI-2 and 111-AB-SI-2, respectively, which are lower than for CGT (8.364 THZ),<sup>27</sup> as shown in Figures 7a,b

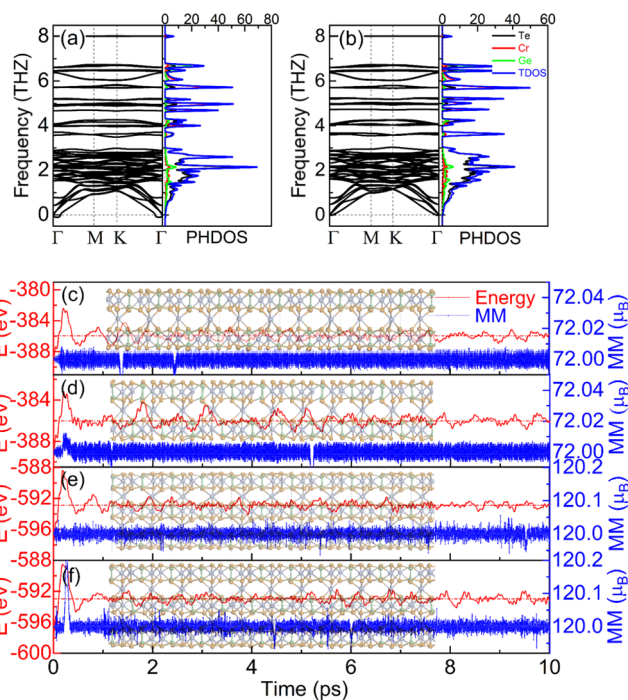


**Figure 7.** Phonon band structures and density of state of CGT: (a) 111-AA-SI-2 and (b) 111-AB-SI-2. Energy and magnetic moment of (c) 111-AA-SI-2 and (d) 111-AB-SI-2 change with time at 300 K. The black, red, green, and blue colors represent Te, Cr, Ge, and total phonon density of the states. The inset shows the snapshots in the simulation. (e) Energy and magnetic moment of (e) 111-AA-SI-3 and (f) 111-AB-SI-3 change with time at 300 K.

and S14. From Figure 7b, we can find that the Te atoms make the main contribution to the low frequency ( $0 < \epsilon < 3.03$  THZ). On the contrary, the high frequency ( $6.3 < \epsilon < 8.06$  THZ) is mainly contributed by Ge atoms, and Cr atoms make the main contribution to the middle frequency ( $3.03 < \epsilon < 6.3$  THZ). 111-AA-SI-2 and 111-AB-SI-2 show a similar trend, as shown in Figure 7a,b.

The thermal stability of SI-CGT is evaluated with AIMD, and the corresponding results are shown in Figure 7c-f. 111-AA(SI)- $N$  ( $N = 2,3$ ) are simulated with NVT at 300 K, as shown in Figure 7c-f, respectively. The total energies fluctuate around  $-386.023$ ,  $-386.045$ ,  $-592.876$ , and  $-593.045$  eV. Meanwhile, both 111-AA-SI-2 and 111-AB-SI-2 have no obvious structure destruction in snapshots at 300 K, as shown in Figures S15, 16, respectively. In order to investigate the stability of SI-CGT at high temperatures, the geometries were changed with time at a temperature of 500 K, as shown in Figure S17 in the Supporting Information. The snapshots imply that the geometries are stable at 300 and 500 K, respectively. Additionally, 111-AA-SI-4 and 111-AB-SI-4 are fabricated and the geometries are stable at room temperature, as shown in Figure S18, in the Supporting Information. More results and discussion could be found in the Supporting Information.

**Magnetocrystalline Anisotropy.** In order to clarify the atomic orbital contribution to the MAE, the tight-binding and second-order perturbation theory<sup>27</sup> is used. The MAE of each atom could be evaluated based on the canonical formulation. The MAE could be expressed as the following equation

$$\text{MAE}_i = \left[ \int E_f(E - E_F) [n_i^{[100]}(E) - n_i^{[001]}(E)] \right] \quad (6)$$

where  $\text{MAE}_i$  represents the MAE contributed by the  $i$ th atom.  $n_i^{[100]}(E)$  and  $n_i^{[001]}(E)$  represent the DOS of the  $i$ th atom with EA along [100] and [001] directions, respectively. In addition, the MAE could be rewritten as the sum of  $\text{MAE}_i$ , as shown in the following equation

$$\text{MAE}_{\text{tot}} = \sum_i \text{MAE}_i \quad (7)$$

Based on the second-order perturbation theory,<sup>71</sup> the MAE could be evaluated by the sum of the following terms

$$\begin{aligned} \Delta E^{--} &= E_x^{--} - E_z^{--} \\ &= \xi^2 \sum_{o^+, u^-} (|\langle o^- | L_z | u^- \rangle|^2 - |\langle o^- | L_x | u^- \rangle|^2) / (E_u^- - E_o^-) \end{aligned} \quad (8)$$

$$\begin{aligned} \Delta E^{-+} &= E_x^{-+} - E_z^{-+} \\ &= \xi^2 \sum_{o^+, u^-} (|\langle o^+ | L_z | u^- \rangle|^2 - |\langle o^+ | L_x | u^- \rangle|^2) / (E_u^- - E_o^-) \end{aligned} \quad (9)$$

where + and – represent spin- $\alpha$  and spin- $\beta$  electron states, and  $\xi$ ,  $L_x$ , and  $L_z$  are the SOC constant, and angular momentum operators along [100] and [001] directions, respectively.  $u$  and  $o$  represent unoccupied and occupied states, and the corresponding  $E_o$  and  $E_u$  represent the energies of occupied and unoccupied states, respectively. According to the above equations, the MAE mainly comes from the contribution of spin-orbital matrix elements and energy difference. The matrix element differences  $|\langle o^- | L_z | u^- \rangle|^2 - |\langle o^- | L_x | u^- \rangle|^2$  and  $|\langle o^+ | L_z | u^- \rangle|^2 - |\langle o^+ | L_x | u^- \rangle|^2$  for p and d orbitals were calculated as shown in Tables 1 and 2, respectively. In order to analyze the change in MAE with stacking orders, the atom-orbital-resolved MAE was calculated, as shown in Figures 8a–l and S19.

**Table 1. Matrix Differences for p Orbitals between EA along [001] and [100] Directions Using Equations 8 and 9**

$u^-$	$o^+$			$o^-$		
	$p_y$	$p_z$	$p_x$	$p_y$	$p_z$	$p_x$
$p_y$	0	1	-1	0	-1	1
$p_z$	1	0	0	-1	0	0
$p_x$	-1	0	0	1	0	0

It can be concluded that the MAE of 111-AA(AB)-2 without  $\text{Cr}_{\text{SI}}$  atoms and 111-AA(AB)-SI-2 mainly comes from Cr and Te atoms' contributions, as shown in Figure 8a–d, i–l. However, it partially comes from Ge's contribution, as shown in Figure 8e–h. The total MAE of 111-AA(AB)-2 is 1.80

(1.91) meV/f.u. and Ge atoms contribute 0.015 (0.019) meV, while Cr atoms contribute 0.698 (0.698) meV, shown in Figure 8a,b,e,f. However, Te atoms in 111-AA(AB)-2 contribute 1.08 and 1.32 meV, respectively. The hybridization between Te's  $p_y$  and  $p_z$  orbitals of 111-AA-2, which corresponds to the matrix difference 1 for p orbitals, tends toward PMA (6.86 meV), as shown in Table 1. However, the hybridization between Te's  $p_y$  and  $p_x$  orbitals, which corresponds to the matrix difference -1 for p orbitals, tends toward IMA (-5.6 meV).

When  $\text{Cr}_{\text{SI}}$  atoms are covalently bonded with Te atoms, the total MAE of 111-AA-SI-2 is decreased to -0.160 meV/f.u., and Ge atoms contribute -0.082 meV, while Cr atoms contribute 1.011 meV, as shown in Figure 8k,c. The hybridization between Cr's  $d_{yz}$  and  $d_z^2$ ,  $d_{xz}$  and  $d_{xy}$ , and  $d_{x^2-y^2}$  and  $d_{yz}$  orbitals contribute 1.359, 0.75, and 0.75 meV, respectively, to the MAE, which correspond to the matrix differences 3, 4, and 1 for d orbitals, as shown in Table 2, and these d orbitals' hybridization favors PMA. The hybridization between Cr atoms'  $d_{xy}$  and  $d_{x^2-y^2}$ , and  $d_{xz}$  and  $d_{yz}$  orbitals contribute -1.174 and -0.664 meV to the MAE, which correspond to the matrix differences -4 and -1 for d orbitals, respectively. This indicates that this hybridization favors IMA. In a word, the d orbitals make a positive contribution to the MAE, which is similar to the CGT bilayers (Figure 8a,b). In addition, Te atoms contribute -1.086 meV to the total MAE. The hybridization between Te's  $p_y$  and  $p_z$  orbitals tends to PMA (2.240 meV). However, the hybridization between Te atoms'  $p_x$  and  $p_y$  orbitals, and  $p_x$  and  $p_z$  contributes -3.057 and -0.227 meV, respectively, tending to IMA.

For 111-AB-SI-2, the total MAE is 0.428 meV/f.u., in which -0.082 meV is contributed by the Ge atoms, as shown in Figure 8e. The Cr atoms contribute 0.744 meV to the MAE, as shown in Figure 8d. The hybridization between Cr's  $d_{yz}$  and  $d_z^2$ ,  $d_{xz}$  and  $d_{xy}$ , and  $d_{x^2-y^2}$  and  $d_{yz}$  orbitals tends to PMA (1.361, 0.61, and 0.61 meV), as shown in Figure 8d. However, the hybridization between Cr atoms'  $d_{xy}$  and  $d_{x^2-y^2}$  orbitals, and  $d_{xz}$  and  $d_{yz}$  tend to IMA (-1.151 and -0.681 meV, respectively). Compared with 111-AA-SI-2, the Te atoms in 111-AB-SI-2 contribute -1.086 meV to the total MAE and the hybridization between Te's  $p_y$  and  $p_z$  orbitals contributes 1.704 meV, as shown in Figure 8l. However, the hybridization between Te atoms'  $p_x$  and  $p_y$  orbitals, and  $p_x$  and  $p_z$  contributes -2.692 and -0.098 meV to IMA. In 111-AB-2, the hybridization between Te's  $p_y$  and  $p_z$  orbitals contributes 6.98 meV to PMA, while the hybridization between Te's  $p_y$  and  $p_x$  orbitals contributes -5.5 meV to PMA, as shown in Figure 8j. Compared with 111-AB-2, 111-AB-SI-2 shows a different trend. In a word, the Te atoms' contribution to the MAE is obviously reduced, as the hybridization between Te's  $p_y$  and  $p_z$  orbitals, and  $p_y$  and  $p_x$  orbitals is obviously weakened when  $\text{Cr}_{\text{SI}}$  atoms are

**Table 2. Matrix Differences for d Orbitals between Magnetization along [001] and [100] Directions Using Equations 8 and 9**

$u^-$	$o^+$					$o^-$				
	$d_{xy}$	$d_{yz}$	$d_z^2$	$d_{xz}$	$d_{x^2-y^2}$	$d_{xy}$	$d_{yz}$	$d_z^2$	$d_{xz}$	$d_{x^2-y^2}$
$d_{xy}$	0	0	0	1	-4	0	0	0	-1	4
$d_{yz}$	0	0	3	-1	1	0	0	-3	1	-1
$d_z^2$	0	3	0	0	0	0	-3	0	0	0
$d_{xz}$	1	-1	0	0	0	-1	1	0	0	0
$d_{x^2-y^2}$	-4	1	0	0	0	4	-1	0	0	0

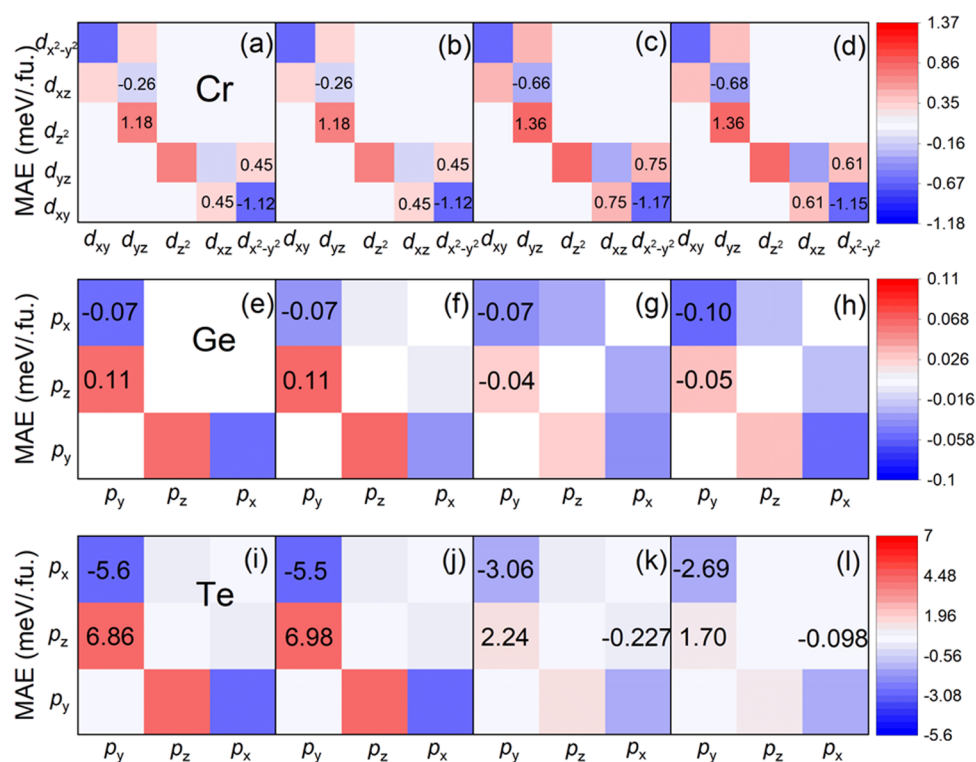


**Figure 8.** (a–d) Cr's d-orbital, (e–h) Ge's p-orbital, and (i–l) Te's p-orbital-resolved MAE of the CGT-AA bilayer, CGT-AB bilayer, CGT-111-AA-SI-2 bilayer, and CGT-111-AB-SI-2 bilayer, respectively.

introduced. Therefore, EA is switched from the original [001] to [100] direction.

The MAE of 111-AA-SI-2 is 0.267 meV larger than 111-AB-SI-2, as shown in Figure 8. The Te and Ge of 111-AA-SI-2 and 111-AB-SI-2 make the same contribution to the total MAE. The difference comes from the Cr atoms' contribution, as shown in Figure 8c,d. The different stacking orders affect the hybridization between Cr atoms'  $d_{xz}$  and  $d_{xy}$ , and  $d_{xy}$  and  $d_{x^2-y^2}$  orbitals, which contribute 0.75, 0.75 meV (111-AA-SI-2), and 0.61, 0.61 meV (111-AB-SI-2), as shown in Figures 3 and 8c,d, respectively.

**Migration Barrier of Cr<sub>SI</sub> Atoms.** The migration barrier for the intercalated Cr atom to move within the interstitial vdW gap in 111-AA(AB)-SI-2 was calculated using the NEB method. The migration barriers of Cr<sub>SI</sub> atoms in 111-AA(AB)-SI-2 are 1.305 and 1.193 eV, as shown in Figure 9a,b, respectively. The Cr<sub>SI</sub> atom migrates from the hollow site (the hollow sites of top and bottom layers) to the nearby hollow site, as shown in Figure 9a,b. The migration barriers of the Cr<sub>SI</sub> atom are high, which implies that Cr<sub>SI</sub> atoms are uneasy to shift from the hollow site to the nearby hollow site. The barrier of 111-AA-SI-2 is higher than that of 111-AB-SI-2, which implies that the migration of the Cr<sub>SI</sub> atom in 111-AA-SI-2 needs more energy to overcome the barrier.

## CONCLUSIONS

In summary, we have systemically investigated the magnetic and electronic properties of SI-CGT. We have found that the interlayer ferromagnetic coupling is enhanced in a self-intercalated system. The SI-CGT bilayers are HMs with interlayer FM order, independent of the stacking orders. The phonon spectrum and AIMD confirm the structural stability of SI-CGT bilayers. The SI-CGT bilayers tend to IMA, and the

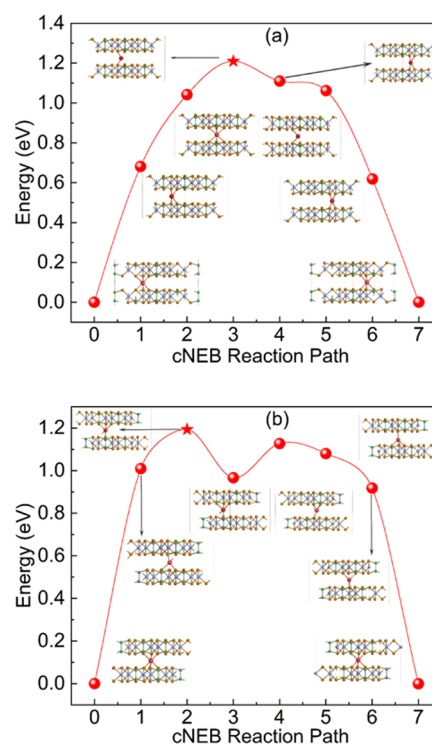


**Figure 9.** Migration barrier of the Cr<sub>SI</sub> atom of (a) 111-AA-SI-2 and (b) 111-AB-SI-2, respectively. The star represents the transition state structures.

MAE of 111-AA-SI-2 and 111-AB-SI-2 is  $-0.160$  and  $-0.428$  meV/f.u., respectively. The orbital-resolved MAEs show that Te's contribution dominates the MAEs of SI-CGT bilayers. The EAs of SI-CGT bilayers are switched from out-of-plane

(CGT bilayers) to in-plane, and because of this switch, the hybridization between Te's  $p_x$  and  $p_y$ , and  $p_y$  and  $p_z$  is obviously weakened. SI-CGTs are HMs with interlayer FM order, independent of  $\text{Cr}_{\text{SI}}$  atoms' concentration. When the films of SI-CGT become thicker ( $N \geq 3$ ), they transform into normal spin-polarized metals with interlayer FM order. The migration barriers of  $\text{Cr}_{\text{SI}}$  atoms in 111-AA(AB)-SI-2 are 1.305 and 1.193 eV, respectively. Our findings provide a new strategy to control the magnetoelectric properties of magnetic vdW materials.

## ■ ASSOCIATED CONTENT

### SI Supporting Information

The Supporting Information is available free of charge at <https://pubs.acs.org/doi/10.1021/acsaelm.2c01749>.

Information on materials, U test on MAE,  $k$ -mesh test, differential charge density of SI-CGT, change of  $\Delta E$  with magnetic orders, band structures of different orders, magnetoelectric properties calculated by DFT-D3, PDOS calculated by HSE06, band structure with SOC, magnetoelectric properties of  $\sqrt{3} \times \sqrt{3} \times 1$  cell, method of MAE calculation, magnetic anisotropy properties of CGT bilayers, PDOS of 111-AA(AB)-3(6) calculated by PBE +  $U$ , PDOS calculated by HSE06, phonon spectrum simulation, snapshots of AIMD at 300 K, AIMD at 500 K, AIMD of four layers, projected MAE of SI-CGT bilayers (PDF)

## ■ AUTHOR INFORMATION

### Corresponding Author

**Zhaoyong Guan** – Key Laboratory of Colloid and Interface Chemistry, Ministry of Education, School of Chemistry and Chemical Engineering, Shandong University, Jinan, Shandong 250100, P. R. China; School of Chemistry and Chemical Engineering, Shandong University, Jinan 250100, P. R. China; [orcid.org/0000-0002-6847-5809](https://orcid.org/0000-0002-6847-5809); Phone: +86-0531-88363179; Email: [zyguan@sdu.edu.cn](mailto:zyguan@sdu.edu.cn); Fax: +86-0531-88363179

### Authors

**Linhui Lv** – School of Chemistry and Chemical Engineering, Shandong University, Jinan 250100, P. R. China

**Ziyuan An** – School of Chemistry and Chemical Engineering, Shandong University, Jinan 250100, P. R. China

**Yanyan Jiang** – Key Laboratory for Liquid-Solid Structural Evolution & Processing of Materials (Ministry of Education), School of Materials Science and Engineering, Shandong University, Jinan, Shandong 250061, P. R. China; [orcid.org/0000-0002-7866-4689](https://orcid.org/0000-0002-7866-4689)

**Ya Su** – School of Electrical Engineering, Shandong University, Jinan, Shandong 250100, P. R. China

Complete contact information is available at: <https://pubs.acs.org/doi/10.1021/acsaelm.2c01749>

### Notes

The authors declare no competing financial interest.

## ■ ACKNOWLEDGMENTS

The authors thank Prof. Wenhui Duan and Xingxing Li for the discussion on the evaluation of MAE and Doctor Rui Li for the discussion on orbital-resolved MAE. They also thank Doctor Yang Li for the discussion on LDA +  $U$ . This work was

supported by the financial support from the Natural Science Foundation of China (Grant No. 11904203) and the Fundamental Research Funds of Shandong University (Grant No. 2019GN065). The authors are grateful to Beijing PARATERA Tech Corp., Ltd. for the computation resource in the National Supercomputer Center of Guangzhou. The scientific calculations in this paper have been done on the HPC Cloud Platform of Shandong University. The authors also acknowledge the Beijing Super Cloud Computing Center (BSCC), Shanghai Supercomputer Center, and Tencent Quantum Laboratory for providing HPC resources.

## ■ REFERENCES

- (1) Golberg, D.; Bando, Y.; Huang, Y.; Terao, T.; Mitome, M.; Tang, C.; Zhi, C. Boron Nitride Nanotubes and Nanosheets. *ACS Nano* **2010**, *4*, 2979–2993.
- (2) Chopra, N. G.; Luyken, R. J.; Cherrey, K.; Crespi, V. H.; Cohen, M. L.; Louie, S. G.; Zettl, A. Boron Nitride Nanotubes. *Science* **1995**, *269*, 966–967.
- (3) Xu, M.; Liang, T.; Shi, M.; Chen, H. Graphene-Like Two-Dimensional Materials. *Chem. Rev.* **2013**, *113*, 3766–3798.
- (4) Wang, Q. H.; Kalantar-Zadeh, K.; Kis, A.; Coleman, J. N.; Strano, M. S. Electronics and Optoelectronics of Two-Dimensional Transition Metal Dichalcogenides. *Nat. Nanotechnol.* **2012**, *7*, 699–712.
- (5) Liao, M. H.; Zang, Y. Y.; Guan, Z. Y.; Li, H. W.; Gong, Y.; Zhu, K. J.; Hu, X. P.; Zhang, D.; Xu, Y.; Wang, Y. Y.; He, K.; Ma, X. C.; Zhang, S. C.; Xue, Q. K. Superconductivity in Few-Layer Stanene. *Nat. Phys.* **2018**, *14*, 344.
- (6) Butler, S. Z.; Hollen, S. M.; Cao, L.; Cui, Y.; Gupta, J. A.; Gutierrez, H. R.; Heinz, T. F.; Hong, S. S.; Huang, J.; Ismach, A. F.; Johnston-Halperin, E.; Kuno, M.; Plashnitsa, V. V.; Robinson, R. D.; Ruoff, R. S.; Salahuddin, S.; Shan, J.; Shi, L.; Spencer, M. G.; Terrones, M.; Windl, W.; Goldberger, J. E. Progress, Challenges, and Opportunities in Two-Dimensional Materials Beyond Graphene. *ACS Nano* **2013**, *7*, 2898–2926.
- (7) Novoselov, K. S.; Mishchenko, A.; Carvalho, A.; Castro Neto, A. H. 2D Materials and Van Der Waals Heterostructures. *Science* **2016**, *353*, No. aac9439.
- (8) Mermin, N. D.; Wagner, H. Absence of Ferromagnetism or Antiferromagnetism in One- or 2-Dimensional Isotropic Heisenberg Models. *Phys. Rev. Lett.* **1966**, *17*, 1133.
- (9) Li, H.; Ruan, S.; Zeng, Y. J. Intrinsic Van Der Waals Magnetic Materials from Bulk to the 2D Limit: New Frontiers of Spintronics. *Adv. Mater.* **2019**, *31*, No. e1900065.
- (10) Gong, C.; Li, L.; Li, Z.; Ji, H.; Stern, A.; Xia, Y.; Cao, T.; Bao, W.; Wang, C.; Wang, Y.; Qiu, Z. Q.; Cava, R. J.; Louie, S. G.; Xia, J.; Zhang, X. Discovery of Intrinsic Ferromagnetism in Two-Dimensional Van Der Waals Crystals. *Nature* **2017**, *546*, 265–269.
- (11) Guan, Z. Y.; Luo, N. N.; Ni, S.; Hu, S. L. Tunable Electronic and Magnetic Properties of Monolayer and Bilayer Janus  $\text{Cr}_2\text{Cl}_3\text{I}_3$ : A First-Principles Study. *Mater. Adv.* **2020**, *1*, 244–253.
- (12) Huang, B.; Clark, G.; Klein, D. R.; MacNeill, D.; Navarro-Moratalla, E.; Seyler, K. L.; Wilson, N.; McGuire, M. A.; Cobden, D. H.; Xiao, D.; Yao, W.; Jarillo-Herrero, P.; Xu, X. Electrical Control of 2D Magnetism in Bilayer  $\text{CrI}_3$ . *Nat. Nanotechnol.* **2018**, *13*, 544–548.
- (13) Luo, C. B.; Peng, X. Y.; Qu, J. F.; Zhong, J. X. Valley Degree of Freedom in Ferromagnetic Janus Monolayer H-VSSe and the Asymmetry-Based Tuning of the Valleytronic Properties. *Phys. Rev. B* **2020**, *101*, No. 245416.
- (14) Zhong, D.; Seyler, K. L.; Linpeng, X.; Cheng, R.; Sivadas, N.; Huang, B.; Schmidgall, E.; Taniguchi, T.; Watanabe, K.; McGuire, M. A.; Yao, W.; Xiao, D.; Fu, K. C.; Xu, X. Van Der Waals Engineering of Ferromagnetic Semiconductor Heterostructures for Spin and Valleytronics. *Sci. Adv.* **2017**, *3*, No. e1603113.
- (15) Jiang, S.; Li, L.; Wang, Z.; Mak, K. F.; Shan, J. Controlling Magnetism in 2D  $\text{CrI}_3$  by Electrostatic Doping. *Nat. Nanotechnol.* **2018**, *13*, 549–553.

- (16) Guan, Z. Y.; Ni, S. Strain-Controllable High Curie Temperature and Magnetic Crystal Anisotropy in a 2D Ferromagnetic Semiconducting  $\text{FeI}_3$  Monolayer. *ACS Appl. Electron. Mater.* **2021**, *3*, 3147–3157.
- (17) Guan, Z.; Ni, S. Prediction of High Curie Temperature, Large Magnetic Crystal Anisotropy, and Carrier Doping-Induced Half-Metallicity in Two-Dimensional Ferromagnetic  $\text{FeX}_3$  ( $X = \text{F}, \text{Cl}, \text{Br}$ , and  $\text{I}$ ) Monolayers. *J. Phys. Chem. C* **2021**, *125*, 16700–16710.
- (18) Fei, Z.; Huang, B.; Malinowski, P.; Wang, W.; Song, T.; Sanchez, J.; Yao, W.; Xiao, D.; Zhu, X.; May, A. F.; Wu, W.; Cobden, D. H.; Chu, J. H.; Xu, X. Two-Dimensional Itinerant Ferromagnetism in Atomically Thin  $\text{Fe}_3\text{GeTe}_2$ . *Nat. Mater.* **2018**, *17*, 778–782.
- (19) Deng, Y.; Yu, Y.; Song, Y.; Zhang, J.; Wang, N. Z.; Sun, Z.; Yi, Y.; Wu, Y. Z.; Wu, S.; Zhu, J.; Wang, J.; Chen, X. H.; Zhang, Y. Gate-Tunable Room-Temperature Ferromagnetism in Two-Dimensional  $\text{Fe}_3\text{GeTe}_2$ . *Nature* **2018**, *563*, 94–99.
- (20) Guo, Y.; Deng, H.; Sun, X.; Li, X.; Zhao, J.; Wu, J.; Chu, W.; Zhang, S.; Pan, H.; Zheng, X.; Wu, X.; Jin, C.; Wu, C.; Xie, Y. Modulation of Metal and Insulator States in 2D Ferromagnetic  $\text{VS}_2$  by Van Der Waals Interaction Engineering. *Adv. Mater.* **2017**, *29*, 1700715.
- (21) van Efferen, C.; Berges, J.; Hall, J.; van Loon, E.; Kraus, S.; Schobert, A.; Wekking, T.; Huttmann, F.; Ploor, E.; Rothenbach, N.; Ollefs, K.; Arruda, L. M.; Brookes, N.; Schonhoff, G.; Kummer, K.; Wende, H.; Wehling, T.; Michely, T. A Full Gap above the Fermi Level: The Charge Density Wave of Monolayer  $\text{VS}_2$ . *Nat. Commun.* **2021**, *12*, No. 6837.
- (22) Bonilla, M.; Kolekar, S.; Ma, Y.; Diaz, H. C.; Kalappattil, V.; Das, R.; Eggers, T.; Gutierrez, H. R.; Phan, M. H.; Batzill, M. Strong Room-Temperature Ferromagnetism in  $\text{VSe}_2$  Monolayers on Van Der Waals Substrates. *Nat. Nanotechnol.* **2018**, *13*, 289–293.
- (23) Guan, Z.; Ni, S. Predicted 2D Ferromagnetic Janus  $\text{VSeTe}$  Monolayer with High Curie Temperature, Large Valley Polarization and Magnetic Crystal Anisotropy. *Nanoscale* **2020**, *12*, 22735–22742.
- (24) Guan, Z.; Ni, S. Strain-Controllable High Curie Temperature, Large Valley Polarization, and Magnetic Crystal Anisotropy in a 2D Ferromagnetic Janus  $\text{VSeTe}$  Monolayer. *ACS Appl. Mater. Interfaces* **2020**, *12*, 53067–53075.
- (25) Yang, D. F.; Yao, W.; Chen, Q. F.; Peng, K. L.; Jiang, P. F.; Lu, X.; Uher, C.; Yang, T.; Wang, G. Y.; Zhou, X. Y.  $\text{Cr}_2\text{Ge}_2\text{Te}_6$ : High Thermoelectric Performance from Layered Structure with High Symmetry. *Chem. Mater.* **2016**, *28*, 1611–1615.
- (26) Ostwal, V.; Shen, T.; Appenzeller, J. Efficient Spin-Orbit Torque Switching of the Semiconducting Van Der Waals Ferromagnet  $\text{Cr}_2\text{Ge}_2\text{Te}_6$ . *Adv. Mater.* **2020**, *32*, No. e1906021.
- (27) An, Z. Y.; Su, Y.; Ni, S.; Guan, Z. Y. Carrier Doping Modulates 2D Intrinsic Ferromagnetic  $\text{Mn}_2\text{Ge}_2\text{Te}_6$  Monolayer, High Curie Temperature, Large Magnetic Crystal Anisotropy. *J. Phys. Chem. C* **2022**, *126*, 11330–11340.
- (28) Ilyas, A.; Wu, H.; Usman, T.; Khan, S. A.; Deng, R. The Induction of Half-Metallicity and Enhanced Ferromagnetism in a  $\text{Cr}_2\text{Ge}_2\text{Te}_6$  Monolayer Via Electron Doping and Alkali Metal Adsorption. *J. Mater. Chem. C* **2021**, *9*, 5952–5960.
- (29) Ilyas, A.; Xiang, S.; Chen, M.; Khan, M. Y.; Bai, H.; He, P.; Lu, Y.; Deng, R. Nonvolatile Electrical Control of 2D  $\text{Cr}_2\text{Ge}_2\text{Te}_6$  and Intrinsic Half Metallicity in Multiferroic Hetero-Structures. *Nanoscale* **2021**, *13*, 1069–1076.
- (30) Ríos-Vargas, V.; Ponce-Pérez, R.; Moreno-Armenta, M. G.; Guerrero-Sánchez, J.  $\text{Cr}_2\text{Ge}_2\text{Te}_6$  Nanoribbons with Perpendicular Magnetic Anisotropy and Half Metallicity: A DFT Study. *J. Phys. D: Appl. Phys.* **2022**, *55*, No. 485003.
- (31) Sivadas, N.; Okamoto, S.; Xu, X.; Fennie, C. J.; Xiao, D. Stacking-Dependent Magnetism in Bilayer  $\text{CrI}_3$ . *Nano Lett.* **2018**, *18*, 7658–7664.
- (32) Wan, J.; Lacey, S. D.; Dai, J.; Bao, W.; Fuhrer, M. S.; Hu, L. Tuning Two-Dimensional Nanomaterials by Intercalation: Materials, Properties and Applications. *Chem. Soc. Rev.* **2016**, *45*, 6742–6765.
- (33) Li, Y.; Li, J.; Li, Y.; Ye, M.; Zheng, F.; Zhang, Z.; Fu, J.; Duan, W.; Xu, Y. High-Temperature Quantum Anomalous Hall Insulators in Lithium-Decorated Iron-Based Superconductor Materials. *Phys. Rev. Lett.* **2020**, *125*, No. 086401.
- (34) Ye, J. T.; Zhang, Y. J.; Akashi, R.; Bahramy, M. S.; Arita, R.; Iwasa, Y. Superconducting Dome in a Gate-Tuned Band Insulator. *Science* **2012**, *338*, 1193–1196.
- (35) Xiong, F.; Wang, H.; Liu, X.; Sun, J.; Brongersma, M.; Pop, E.; Cui, Y. Li Intercalation in  $\text{MoS}_2$ : In Situ Observation of Its Dynamics and Tuning Optical and Electrical Properties. *Nano Lett.* **2015**, *15*, 6777–6784.
- (36) Ou, J. Z.; Chrimes, A. F.; Wang, Y.; Tang, S. Y.; Strano, M. S.; Kalantar-zadeh, K. Ion-Driven Photoluminescence Modulation of Quasi-Two-Dimensional  $\text{MoS}_2$  Nanoflakes for Applications in Biological Systems. *Nano Lett.* **2014**, *14*, 857–863.
- (37) Yao, J.; Koski, K. J.; Luo, W.; Cha, J. J.; Hu, L.; Kong, D.; Narasimhan, V. K.; Huo, K.; Cui, Y. Optical Transmission Enhancement through Chemically Tuned Two-Dimensional Bismuth Chalcogenide Nanoplates. *Nat. Commun.* **2014**, *5*, No. 5670.
- (38) Wang, M.; Koski, K. J. Reversible Chemochromic  $\text{MoO}_3$  Nanoribbons through Zerovalent Metal Intercalation. *ACS Nano* **2015**, *9*, 3226–3233.
- (39) Acerce, M.; Voiry, D.; Chhowalla, M. Metallic It Phase  $\text{MoS}_2$  Nanosheets as Supercapacitor Electrode Materials. *Nat. Nanotechnol.* **2015**, *10*, 313.
- (40) Wan, J. Y.; Bao, W. Z.; Liu, Y.; Dai, J. Q.; Shen, F.; Zhou, L. H.; Cai, X. H.; Urban, D.; Li, Y. Y.; Jungjohann, K.; Fuhrer, M. S.; Hu, L. B. In Situ Investigations of  $\text{Li-MoS}_2$  with Planar Batteries. *Adv. Energy Mater.* **2015**, *5*, No. 1401742.
- (41) Wang, H.; Lu, Z.; Xu, S.; Kong, D.; Cha, J. J.; Zheng, G.; Hsu, P. C.; Yan, K.; Bradshaw, D.; Prinz, F. B.; Cui, Y. Electrochemical Tuning of Vertically Aligned  $\text{MoS}_2$  Nanofilms and Its Application in Improving Hydrogen Evolution Reaction. *Proc. Natl. Acad. Sci. U.S.A.* **2013**, *110*, 19701.
- (42) Huang, M.; Ma, Z. W.; Wang, S.; Li, S.; Li, M.; Xiang, J. X.; Liu, P.; Hu, G. J.; Zhang, Z. M.; Sun, Z.; Lu, Y. L.; Sheng, Z. G.; Chen, G.; Chueh, Y. L.; Yang, S. Y.; Xiang, B. Significant Perpendicular Magnetic Anisotropy in Room-Temperature Layered Ferromagnet of Cr-Intercalated  $\text{CrTe}_2$ . *2D Mater.* **2021**, *8*, No. 031003.
- (43) Wang, N.; Tang, H.; Shi, M.; Zhang, H.; Zhuo, W.; Liu, D.; Meng, F.; Ma, L.; Ying, J.; Zou, L.; Sun, Z.; Chen, X. Transition from Ferromagnetic Semiconductor to Ferromagnetic Metal with Enhanced Curie Temperature in  $\text{Cr}_2\text{Ge}_2\text{Te}_6$  Via Organic Ion Intercalation. *J. Am. Chem. Soc.* **2019**, *141*, 17166–17173.
- (44) Weber, D.; Trout, A. H.; McComb, D. W.; Goldberger, J. E. Decomposition-Induced Room-Temperature Magnetism of the Na-Intercalated Layered Ferromagnet  $\text{Fe}_{3-x}\text{GeTe}_2$ . *Nano Lett.* **2019**, *19*, 5031–5035.
- (45) Huang, X. K.; Xu, J. L.; Zeng, R. F.; Jiang, Q. L.; Nie, X.; Chen, C.; Jiang, X. P.; Liu, J. M. Li-Ion Intercalation Enhanced Ferromagnetism in Van Der Waals  $\text{Fe}_3\text{GeTe}_2$  Bilayer. *Appl. Phys. Lett.* **2021**, *119*, 012405.
- (46) Huang, X. K.; Xu, J. L.; Nie, X.; Chen, C.; Wang, W.; Song, G.; Jiang, X. P.; Liu, J. M. Significantly Enhanced Interlayer Ferromagnetic Coupling in Van Der Waals  $\text{Fe}_3\text{GeTe}_2$  Bilayer by Be-Ion Intercalation. *Appl. Phys. Lett.* **2022**, *120*, 073106.
- (47) Yao, Y. Y.; Wen, Y.; Wang, F.; Li, N. N.; Wang, J. J.; Wang, Y. R.; Yang, J.; Zhan, X. Y.; Wang, Z. X.; He, J. Self-Intercalated Two-Dimensional Magnetic Semiconductor  $\text{V}_8(\text{S}_{1-x}\text{Se}_x)_{15}$ . *Appl. Phys. Lett.* **2021**, *118*, 221903.
- (48) Coughlin, A. L.; Xie, D.; Zhan, X.; Yao, Y.; Deng, L.; Hewa-Walpitage, H.; Bontke, T.; Chu, C. W.; Li, Y.; Wang, J.; Fertig, H. A.; Zhang, S. Van Der Waals Superstructure and Twisting in Self-Intercalated Magnet with near Room-Temperature Perpendicular Ferromagnetism. *Nano Lett.* **2021**, *21*, 9517–9525.
- (49) Huang, M.; Gao, L.; Zhang, Y.; Lei, X.; Hu, G.; Xiang, J.; Zeng, H.; Fu, X.; Zhang, Z.; Chai, G.; Peng, Y.; Lu, Y.; Du, H.; Chen, G.; Zang, J.; Xiang, B. Possible Topological Hall Effect above Room Temperature in Layered  $\text{Cr}_{1.2}\text{Te}_2$  Ferromagnet. *Nano Lett.* **2021**, *21*, 4280–4286.

(50) Zhao, X.; Song, P.; Wang, C.; Riis-Jensen, A. C.; Fu, W.; Deng, Y.; Wan, D.; Kang, L.; Ning, S.; Dan, J.; Venkatesan, T.; Liu, Z.; Zhou, W.; Thygesen, K. S.; Luo, X.; Pennycook, S. J.; Loh, K. P. Engineering Covalently Bonded 2D Layered Materials by Self-Intercalation. *Nature* **2020**, *581*, 171–177.

(51) Xiong, Y. M. Engineering Two-Dimensional Magnets at Birth. *Nat. Electron.* **2022**, *5*, 197–198.

(52) Li, R.; Jiang, J. W.; Bai, H. L.; Mi, W. B. Tailoring Interlayer Magnetic Coupling to Modify the Magnetic Properties of FeCl<sub>2</sub> Bilayers by Self-Intercalation. *J. Mater. Chem. C* **2022**, *10*, 14955–14962.

(53) Tang, B. J.; Wang, X. W.; Han, M. J.; Xu, X. D.; Zhang, Z. W.; Zhu, C.; Cao, X.; Yang, Y. M.; Fu, Q. D.; Yang, J. Q.; Li, X. J.; Gao, W. B.; Zhou, J. D.; Lin, J. H.; Liu, Z. Phase Engineering of Cr<sub>5</sub>Te<sub>8</sub> with Colossal Anomalous Hall Effect. *Nat. Electron.* **2022**, *5*, 224–232.

(54) Zhang, H. X.; Rousuli, A.; Zhang, K. N.; Luo, L. P.; Guo, C. G.; Cong, X.; Lin, Z. Z.; Bao, C. H.; Zhang, H. Y.; Xu, S. N.; Feng, R. F.; Shen, S. C.; Zhao, K.; Yao, W.; Wu, Y.; Ji, S. H.; Chen, X.; Tan, P. H.; Xue, Q. K.; Xu, Y.; Duan, W. H.; Yu, P.; Zhou, S. Y. Tailored Ising Superconductivity in Intercalated Bulk NbSe<sub>2</sub>. *Nat. Phys.* **2022**, *18*, 1425–1430.

(55) Zhang, X.; Liu, W.; Niu, W.; Lu, Q.; Wang, W.; Sarikhani, A.; Wu, X.; Zhu, C.; Sun, J.; Vaninger, M.; Miceli, P. F.; Li, J.; Singh, D. J.; Hor, Y. S.; Zhao, Y.; Liu, C.; He, L.; Zhang, R.; Bian, G.; Yu, D.; Xu, Y. Self-Intercalation Tunable Interlayer Exchange Coupling in a Synthetic Van Der Waals Antiferromagnet. *Adv. Funct. Mater.* **2022**, *32*, No. 2202977.

(56) Zhang, C.; Liu, C.; Zhang, J.; Yuan, Y.; Wen, Y.; Li, Y.; Zheng, D.; Zhang, Q.; Hou, Z.; Yin, G.; Liu, K.; Peng, Y.; Zhang, X.-X. Room-Temperature Magnetic Skyrmions and Large Topological Hall Effect in Chromium Telluride Engineered by Self-Intercalation. *Adv. Mater.* **2023**, *35*, No. 2205967.

(57) Kresse, G.; Furthmüller, J. Efficiency of Ab-Initio Total Energy Calculations for Metals and Semiconductors Using a Plane-Wave Basis Set. *Comput. Mater. Sci.* **1996**, *6*, 15–50.

(58) Perdew, J. P.; Burke, K.; Ernzerhof, M. Generalized Gradient Approximation Made Simple. *Phys. Rev. Lett.* **1996**, *77*, 3865–3868.

(59) Liechtenstein, A. I.; Anisimov, V. V.; Zaanen, J. Density-Functional Theory and Strong Interactions: Orbital Ordering in Mott-Hubbard Insulators. *Phys. Rev. B* **1995**, *52*, R5467–R5470.

(60) Heyd, J.; Scuseria, G. E.; Ernzerhof, M. Erratum: “Hybrid Functionals Based on a Screened Coulomb Potential” [*J. Chem. Phys.* **118**, 8207 (2003)]. *J. Chem. Phys.* **2006**, *124*, 219906.

(61) Heyd, J.; Scuseria, G. E.; Ernzerhof, M. Hybrid Functionals Based on a Screened Coulomb Potential. *J. Chem. Phys.* **2003**, *118*, 8207–8215.

(62) Baranava, M. S.; Hvazdouski, D. C.; Skachkova, V. A.; Stempitsky, V. R.; Danilyuk, A. L. Magnetic Interactions in Cr<sub>2</sub>Ge<sub>2</sub>Te<sub>6</sub> and Cr<sub>2</sub>Si<sub>2</sub>Te<sub>6</sub> Monolayers: Ab Initio Study. *Mater. Today: Proc.* **2020**, *20*, 342–347.

(63) Tang, C.; Zhang, L.; Sanvito, S.; Du, A. Electric-Controlled Half-Metallicity in Magnetic Van Der Waals Heterobilayer. *J. Mater. Chem. C* **2020**, *8*, 7034–7040.

(64) Monkhorst, H. J.; Pack, J. D. Special Points for Brillouin-Zone Integrations. *Phys. Rev. B* **1976**, *13*, 5188–5192.

(65) Togo, A.; Tanaka, I. First Principles Phonon Calculations in Materials Science. *Scr. Mater.* **2015**, *108*, 1–5.

(66) Nosé, S. A Unified Formulation of the Constant Temperature Molecular Dynamics Methods. *J. Chem. Phys.* **1984**, *81*, 511–519.

(67) Grimme, S. Semiempirical GGA-Type Density Functional Constructed with a Long-Range Dispersion Correction. *J. Comput. Chem.* **2006**, *27*, 1787–1799.

(68) Grimme, S.; Antony, J.; Ehrlich, S.; Krieg, H. A Consistent and Accurate Ab Initio Parametrization of Density Functional Dispersion Correction (DFT-D) for the 94 Elements H-Pu. *J. Chem. Phys.* **2010**, *132*, No. 154104.

(69) Henkelman, G.; Uberuaga, B. P.; Jonsson, H. A Climbing Image Nudged Elastic Band Method for Finding Saddle Points and Minimum Energy Paths. *J. Chem. Phys.* **2000**, *113*, 9901–9904.

(70) Henkelman, G.; Arnaldsson, A.; Jónsson, H. A Fast and Robust Algorithm for Bader Decomposition of Charge Density. *Comput. Mater. Sci.* **2006**, *36*, 354–360.

(71) Wang, D.-s.; Wu, R.; Freeman, A. J. First-Principles Theory of Surface Magnetocrystalline Anisotropy and the Diatomic-Pair Model. *Phys. Rev. B* **1993**, *47*, 14932–14947.

## Recommended by ACS

### Nano-Patterned Magnetic Edges in CrGeTe<sub>3</sub> for Quasi 1-D Spintronic Devices

Avia Noah, Yonathan Anahory, *et al.*

MAY 11, 2023  
ACS APPLIED NANO MATERIALS

READ 

### Control of Compensation Temperature in CoGd Films through Hydrogen and Oxygen Migration under Gate Voltage

Xue Ren, Jifan Hu, *et al.*

JUNE 22, 2023  
NANO LETTERS

READ 

### Anisotropic Magnetoresistance and Planar Hall Effect in Layered Room-Temperature Ferromagnet Cr<sub>1.2</sub>Te<sub>2</sub>

Xiang Ma, Bin Xiang, *et al.*

MAY 03, 2023  
ACS APPLIED ELECTRONIC MATERIALS

READ 

### Enhanced Room Temperature Ferromagnetism in Highly Strained 2D Semiconductor Cr<sub>2</sub>Ge<sub>2</sub>Te<sub>6</sub>

Adam O'Neill, Jan Seidel, *et al.*

DECEMBER 22, 2022  
ACS NANO

READ 

Get More Suggestions >